JACS
JOURNAL OF THE AMERICAN CHEMICAL SOCIETY

Article

pubs.acs.org/JACS

Role of Substrate Positioning in the Catalytic Reaction of 4-Hydroxyphenylpyruvate Dioxygenase—A QM/MM Study

Anna Wójcik,[†,‡] Ewa Broclawik,[†] Per E. M. Siegbahn,[§] Marcus Lundberg,[∥] Graham Moran,[⊥] and Tomasz Borowski*[,†]

[†]Jerzy Haber Institute of Catalysis and Surface Chemistry, Polish Academy of Sciences, ul. Niezapominajek 8, 30-239 Cracow, Poland

[‡]Department of Computational Biophysics and Bioinformatics, Faculty of Biochemistry, Biophysics and Biotechnology, Jagiellonian University, ul. Gronostajowa 7, 30-387 Cracow, Poland

[§]Department of Organic Chemistry, Stockholm University, S-106 91, Stockholm, Sweden

[∥]Ångstrom Laboratory, Department of Chemistry, Uppsala University, Box 518, SE-751 20 Uppsala, Sweden

[⊥]Department of Chemistry and Biochemistry, University of Wisconsin—Milwaukee, 3210 North Cramer Street, Milwaukee, Wisconsin 53211-3209, United States

Supporting Information

ABSTRACT: Ring hydroxylation and coupled rearrangement reactions catalyzed by 4-hydroxyphenylpyruvate dioxygenase were studied with the QM/MM method ONIOM(B3LYP:AMBER). For electrophilic attack of the ferryl species on the aromatic ring, five channels were considered: attacks on the three ring atoms closest to the oxo ligand (C1, C2, C6) and insertion of oxygen across two bonds formed by them (C1−C2, C1−C6). For the subsequent migration of the carboxymethyl substituent, two possible directions were tested (C1→C2, C1→C6), and two different mechanisms were sought (stepwise radical, single-step heterolytic). In addition, formation of an epoxide (side)product and benzylic hydroxylation, as catalyzed by the closely related hydroxymandelate synthase, were investigated. From the computed reaction free energy profiles it follows that the most likely mechanism of 4-hydroxyphenylpyruvate dioxygenase involves electrophilic attack on the C1 carbon of the ring and subsequent single-step heterolytic migration of the substituent. Computed values of the kinetic isotope effect for this step are inverse, consistent with available experimental data. Electronic structure arguments for the preferred mechanism of attack on the ring are also presented.

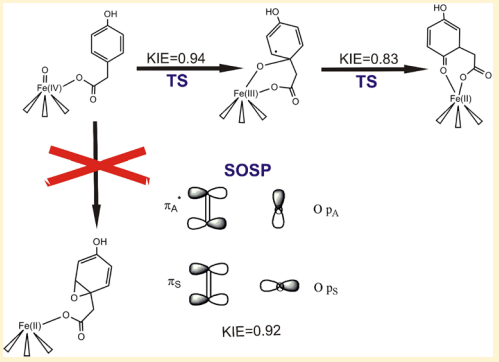

1. INTRODUCTION

4-Hydroxyphenylpyruvate dioxygenase (HPPD) together with the related hydroxymandelate synthase (HMS) belong to a family of α-ketoacid-dependent dioxygenases. However, they do not require the usual cosubstrate, i.e., α-ketoglutarate, because their substrate, 4-hydroxyphenylpyruvate (HPP), contains a built-in α-ketoacid moiety that is used for O_2 activation. Ubiquitous in aerobic forms of life, HPPD is involved in tyrosine catabolism as well as in biosynthesis of plastoquinones and tocopherols, which are essential compounds for the process of photosynthesis. HPPD catalyzes oxidation of HPP to 2,5-dihydroxyphenylacetate (homogentisate, HG), which is the second step in the L-tyrosine catabolic pathway eventually leading to acetoacetate and fumarate.[1,2] Deficiency in HPPD activity results in a rare hereditary metabolic disorder tyrosinemia type III, whereas HPPD inhibitors are used as medicines alleviating symptoms of other genetic inborn diseases related to accumulations of toxic metabolites produced in tyrosine catabolism.[3] In plants, the tyrosine metabolic pathway branches at HG for the biosynthesis of lyophilic cofactors required for photosynthesis,[4] and hence, HPPD inhibitors have herbicidal activity.[3] HMS performs chemistry similar to that of HPPD, the oxidation of HPP to (*S*)-hydroxymandelate (HMA), but is found in only a few strains of bacteria, where HMA is a precursor for the biosynthesis of *p*-hydroxyphenylglycine, a component of macrocyclic peptide antibiotics, such as vancomycin.[5−7] HMS catalyzes oxidation of HPP to HMA, which in the following steps is transformed into *p*-hydroxyphenylglycine.

HPPD and HMS not only share the same substrates, i.e., HPP and O_2, but also exhibit identical structural topology, and it is commonly assumed that for the two enzymes the initial steps of the catalytic reactions are ostensibly the same and yield a common hydroxylating intermediate, i.e., E-Fe(IV)═O-hydroxyphenylacetate species (Figure 1). From this species the catalytic pathway diverges, leading to the enzyme-specific final products. The common part of HMS and HPPD catalytic cycles includes oxidative decarboxylation of the ketoacid moiety and subsequent heterolytic cleavage of the O−O bond, leading to the oxoferryl intermediate.[8] In the following steps hydroxyphenylacetate (HPA) is either converted to HG, via aromatic ring hydroxylation and side-chain rearrangement, or hydroxylated at the

Received: June 25, 2014
Published: August 26, 2014

   dx.doi.org/10.1021/ja506378u | J. Am. Chem. Soc. 2014, 136, 14472−14485

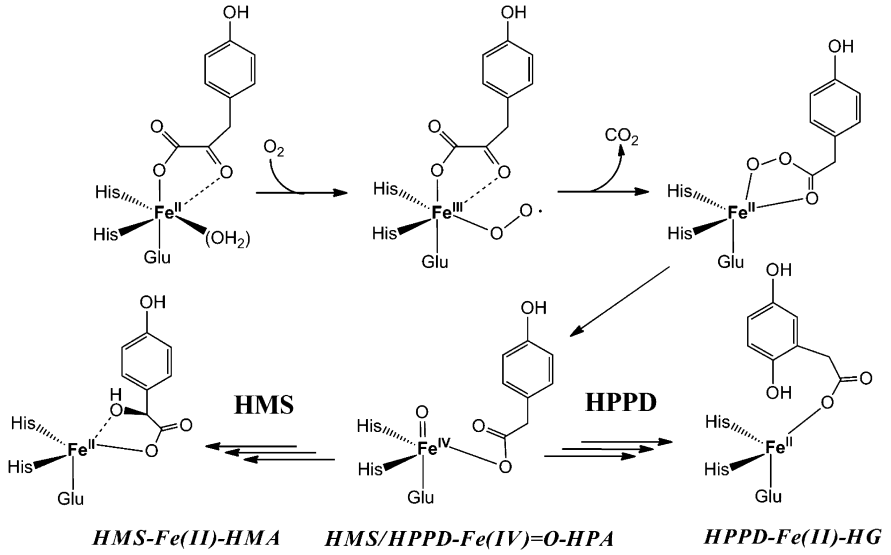

Figure 1. Oxygen activation mechanism proposed for HMS and HPPD.

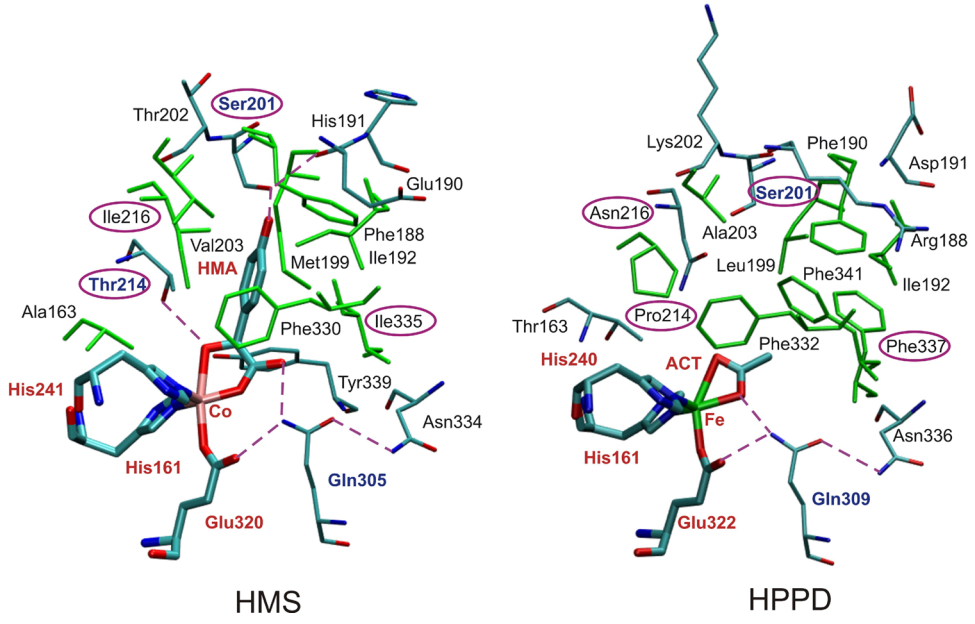

Figure 2. Active sites in X-ray crystal structures of *Amycolatopsis orientalis* HMS-Co(II)-HMA and *Pseudomonas fluorescens* HPPD-Fe(II)-acetate complexes (PDB codes: 2R5V and 1CJX, respectively). Residue names in red are for the first-shell metal ligands; residue names in blue are for the amino acids hydrogen-bonding to the first-shell metal ligands. Ovals mark residues substituted in the mutagenetic studies. Hydrophobic residues are in green.

benzylic carbon producing HMA, which is determined by interactions with second-shell residues.[9] Recently, HMS was successfully engineered to produce (*R*)-hydroxymandelate.[10]

X-ray crystal structures for only the HMS-Co(II)-HMA complex (PDB code: 2R5V),[7] HPPD inhibitor complexes (PDB codes: 1T47, 1SQI, 1TFZ, 1TG5),[11,12] and select other ligands (PDB codes: 1CJX, 3ISQ)[13] have been solved. Thus, the available structural data provide only indirect information on the position of HPP binding within the active sites.

Correlation of the primary and tertiary structures of these enzymes indicates two domains: a poorly conserved (apparently vestigial) N-terminal domain and a more highly conserved C-terminal domain. The catalytic site is located in the C-terminal domain that houses the active cite including a 2-His-1-Glu facial triad responsible for coordinating the Fe(II) cofactor[3] (see Figure 2).

Spectroscopic studies suggest that both HMS and HPPD bind HPP in a bidentate coordination complex that forms between the α-ketoacid and the ferrous ion and that the difference in product specificity arises as a consequence of different orientations of the substrate's aromatic ring in the catalytic site.[7,8,14]

The structure of the HMS-Co(II)-HMA complex shows that HMA is bound to the metal center in a bidentate fashion through its benzylic hydroxyl oxygen and one of the oxygens from its carboxylate group.[7] The first-shell metal ligands create a coordinational trigonal bipyramid, where the equatorial positions are occupied by two histidines (His161, His241) and the carboxylate from the HMA ligand, whereas glutamate (Glu320) and the hydroxyl group of HMA are in the axial positions. HMA is hydrogen-bonded with three amino acids: Ser201, Thr214, and Gln305 (labeled in blue in Figure 2). Ser201 is involved in a H-bond with *p*-hydroxyl group of HMA, Thr214 creates a H-bond

dx.doi.org/10.1021/ja506378u | J. Am. Chem. Soc. 2014, 136, 14472−14485

with the benzylic hydroxyl of HMA, while Gln305 forms a hydrogen-bonding interaction with one of the HMA carboxylate oxygen, as well as with the carboxylate group of Glu320 from the facial triad.[7]

Similarities in sequences, structures, and the reaction mechanisms of HMS and HPPD make these enzymes very attractive targets for mutagenesis experiments aimed at switching the hydroxylation specificity.[15−17] Results of mutagenesis studies showed that HMS is very tolerant to mutations, and single, double, and triple amino acid substitutions at conserved positions have not led to production of HG.[15,16] In the case of HPPD, analogous attempts were more successful, and some mutants produced HMA. These observations might indicate that the HMS reaction is the "default" oxidation process for the (2His-1Glu)-Fe(IV)═O-HPA catalytic core, presumably less controlled by interactions with the second-shell residues than ring hydroxylation specific for HPPD.[15−17] Results reported by Gunsior et al. showed that two HPPD (*S. avermitilis*) single-point mutants, namely Asn216Ile and Phe337Ile, form mixture of products including HG and HMA.[16] It was suggested that structural changes introduced by these point mutations inhibit formation of HG and hence turn on production of the side product, HMA.[15] O'Hare and co-workers found that a relatively large group of double mutants of *P. fluorescens* HPPD exhibit HMS activity, yet HG is always an accompanying product.[15] A majority of such constructs have substitutions at positions 216 and 337 (see Figure 2).[15] Interestingly, some of them, e.g., Asn216Val and Phe337Val, did not affect the reaction specificity when introduced separately, but together induced a partial specificity switch.[15]

In the resting form of HPPD the active-site iron is six-fold coordinated (2-His-1Glu facial triad and three water molecules), as revealed by X-ray crystal structures (PDB codes: 1SP8, 1SP9) and spectroscopic studies.[14,18,19] Results of steady-state kinetics measurements indicated that HPP binds to Fe(II) prior to dioxygen, while CO_2 is the first product released from the active site, similarly to other α-ketoacid-dependent enzymes.[20−22]

Raspail and co-workers performed QM/MM calculations to test the possible binding modes of HPP in the HPPD active site.[23] Different models, created for an *Arabidopsis thaliana* HPPD structure (PDB code: 1SQD), were employed, including models of the E-Fe(II)-HPP and E-Fe(IV)═O-HPA complexes. Two plausible substrate binding modes were taken into consideration in these studies: one proposed by Serre et al. involving interactions between Gln272, Gln286, Gln358, and the substrate, and the second one, proposed by Brownlee et al. and based on the HMS-HMA crystal structure (PDB code: 2R5V),[7,13,23] where Ser246 and Asn261 participate in binding of the substrate. In the first mode, the 4-hydroxyl group of HPP forms hydrogen bonds with Gln225 (272; in parentheses residue numbers for *A. thaliana* HPPD) and Gln239 (286), whereas the Brownlee's mode involves H-bonds between Ser201 (246), Asn216 (261), and the 4-hydroxyl moiety of HPP. In both cases Gln309 (358) forms a H-bond with the carboxylic group of HPP. The QM/MM studies together with mutagenetic and kinetic experiments led to a suggestion that Gln225 (272), Gln239 (286), and Gln309 (358) play important roles in the binding of HPP and the first nucleophilic attack during the catalytic cycle, which leads to a peroxo-bridged intermediate.[23] Raspail and co-workers suggested that, in the subsequent step, the intermediate moves and starts to interact, via its 4-hydroxyl group, with Ser201 (246) and Asn216 (261), and these interactions presumably play a key role in directing the electrophilic attack on the aromatic ring of HPA. Accordingly, substitutions at these positions result in a significant decrease in k_{cat} of HPPD.[7,13]

Previous computational studies also provided some insights into the reaction mechanisms of the two enzymes. Concerning the initial stages of the reaction, it was proposed that the Fe(III)-$O_2^{-\bullet}$ species attacks the carbonyl carbon of HPP.[8] This initiates decarboxylation yielding the Fe(II)-peracid intermediate. Subsequent heterolytic cleavage of the O−O bond produces HPA in complex with the Fe(IV)═O form of the iron cofactor, which is the last common intermediate for HMS and HPPD[8] (Figure 1). Notably, the Fe(IV)═O species has been trapped and characterized by spectroscopic methods for taurine 2-oxoglutarate dioxygenase and two other α-ketoacid-dependent enzymes.[24−26] With respect to the hydroxylation reactions, for HPPD it was proposed that electrophilic attack on the aromatic ring of HPA leads to a high-spin Fe(III)/ring radical σ-complex (see Figure 3).[8,9,14] The subsequent migration of the acetic acid side chain was found to proceed in two steps: first, the C−C bond cleavage leading to the biradical intermediate, and second, a fast rebound of the migrating substituent at the adjacent position in the aromatic ring.[8] The final step of the HPPD catalytic cycle was said to be a tautomerization reaction involving a proton transfer from the sp^3 carbon of the ring to the ketone oxygen and yielding HG. The DFT results indicated that this last process can occur either in solution or in the active site.[8]

Valuable insights into the hydroxylation mechanism of HPPD were provided by results of recent studies by Shah et al., where kinetic isotope effects (KIE) were measured from the product partitioning exhibited by WT and some mutants of *Streptomyces avermitilis* HPPD.[17,27] With ring-deuterated HPP, an inverse secondary KIE of 0.84 was obtained, which was interpreted as evidence for a change of hybridization from sp^2 to sp^3 on the carbon atom(s) directly bound to deuterium, i.e., direct attack of the ferryl species on the C1−C2 bond of the aromatic ring and formation of a 1,2-epoxide.[17] HPPD mutants, such as Asn245Ile, Asn245Gln, Pro243Thr, and Ser230Ala, gave secondary KIE of around 1.[17] In studies using 1′,1′-dideuterio-HPP the KIE value obtained for WT *S. avermitilis* HPPD was 0.990, which was proposed to be consistent with a heterolytic single step mechanism of carboxymethyl migration.[28] However, for the Asn216(245)Ser mutant KIE amounted to 1.39, a value presumably more consistent with the radical two-step migration.[27]

Here we report results of a QM/MM study undertaken with the aim to enhance our understanding of the HPPD reaction steps following generation of the ferryl species. The most important result of this work is the finding that the observed inverse KIE can be explained without invoking substantial hybridization change on the deuterated carbons. The mechanism for hydroxylation and rearrangement supported by the QM/MM results involves electrophilic attack on the substituted ring carbon atom and a single-step migration of the carboxymethyl substituent, similar to the NIH hydride shift.

2. MODELS AND METHODS

2.1. Molecular Dynamics Simulations. MD simulations were performed for the HPPD-Fe(IV)═O-HPA complex in order to obtain a reliable starting structure for QM/MM calculations. The MD model was prepared on the basis of the crystal structure of *Pseudomonas fluorescens* HPPD (PDB code: 1CJX). The residues missing in the crystal structure, i.e., Ala1-Asp2-Leu3 and Asp357, were added with the program Modeller.[29−32] The ferrous ion was substituted with an iron-oxo group, and acetate was replaced by HPA. Protonation states (at pH 7.0) of basic and acidic residues (other than iron ligands) were assigned on the basis of pK_a calculations performed with the PROPKA

dx.doi.org/10.1021/ja506378u | J. Am. Chem. Soc. 2014, 136, 14472−14485

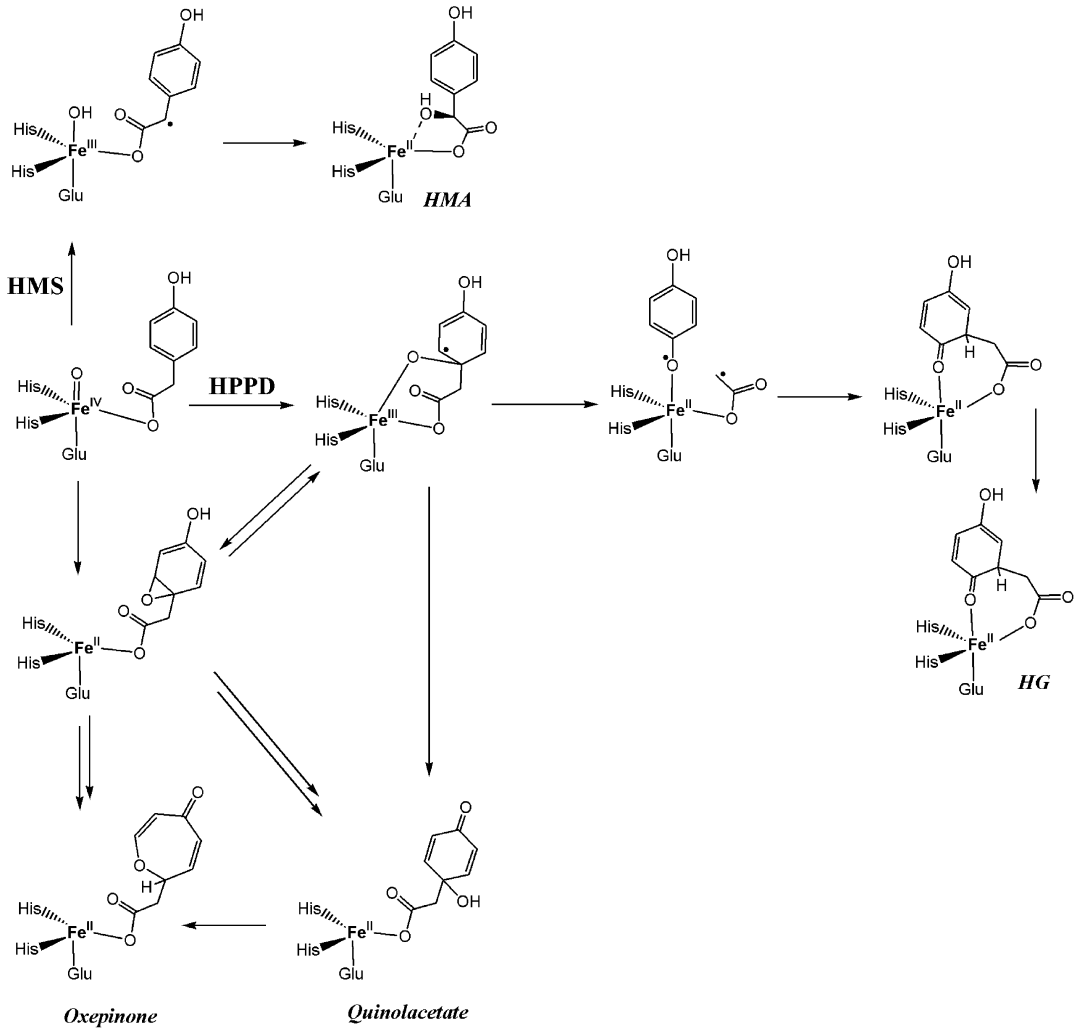

Figure 3. Previously suggested hydroxylation mechanisms for HMS and HPPD and pathways leading to alternative products: oxepinone and quinolacetate.

server,[33,34] with no unexpected protonation states predicted. The positions of the protons in the histidine side chains (Nε or Nδ) were chosen on the basis of visual inspection of the immediate environment in the crystal structure: His103 was doubly protonated; His73 and His164 were protonated on Nδ; and His41, His47, and His281 had Nε protonated. The total charge of the HPPD system obtained in this manner was −14, so to compensate this charge 14 Na^+ ions were added.

Missing force field parameters for the non-heme iron oxoferryl complex were derived from QM calculations in our previous studies.[9] Standard protein residues were described with the ff03 AMBER force field.[35] The solvent was modeled by TIP3P water molecules filling a cube with at least a 10 Å distance between the protein and the face of the cube.[36]

Before the molecular dynamic simulations the system was minimized. In the first step the protein and HPA were restrained with a 500 kcal/(mol·Å^2) harmonic potential, while the water and the Na^+ ion positions were optimized. In the second step the protein was restrained with a 10 kcal/(mol·Å^2) harmonic potential, while in the final step, the minimization of the whole system was performed with no restraints. Each minimization consisted of 500 steps of steepest-descent and additional 4500 steps performed with the conjugate-gradient algorithm. The optimized structure was subsequently heated from 0 to 300 K under constant volume conditions during a 100-ps-long dynamics. In the following step the system was subjected to a 100-ps-long constant pressure dynamics meant to equilibrate the density of the model. The simulations of the heating and constant pressure dynamics were performed with the protein backbone restrained with a force constant of 1 kcal/(mol·Å^2). The final simulations with constant temperature (300 K) and pressure (1 atm), maintained with Langevin dynamics and isotropic position scaling algorithm under periodic boundary conditions, were completed with a 2 fs time step. The SHAKE algorithm was employed to constrain covalent bonds involving H-atoms, and the particle-mesh Ewald method was utilized for the electrostatics. MD simulations spanned in total 24.2 ns and were conducted with the AMBER 11 package.[37]

2.2. QM/MM Models and Methods. For the QM/MM calculations, the ONIOM method implemented in the Gaussian 09 program was used.[38] For the QM part of the system the hybrid exchange correlation functional B3LYP was employed,[39,40] whereas the MM region was described with the AMBER force field. In order to minimize the risk of accidental changes of geometry of the MM part of the system when moving along the reaction coordinate, a snapshot after 14 ns of MD simulation was cooled from 300 to 0 K in an NV = constant 100-ps-long simulation. This structure was used to prepare the ONIOM model, which comprised of 6634 atoms. Water molecules and counterions situated farther than 20 Å away from the active-site iron were removed from the model.

The QM region (84 atoms) included the His161, His240, and Glu322 side chains, HPA, and the Fe(IV)═O group, forming the first coordination shell, as well as the Thr163, Ser201, and Gln309 side chains and one water molecule, all of which were in hydrogen-bonding contacts with the first-shell ligands. Since the water molecule entered the active site during the final stage of the 14.2-ns-long MD simulation, another 10 ns were simulated. The water molecule remained in contact with the first-shell ligands during this additional 10 ns, which suggests it is bound firmly. However, whether this water molecule will be actually bound or not during the reaction steps following formation of Fe(IV)═O will depend on the structure of preceding intermediates

dx.doi.org/10.1021/ja506378u | J. Am. Chem. Soc. 2014, 136, 14472−14485

and/or rate of water transport to the active site. Hence, a model lacking this second-shell water was also tested.

For the amino acid ligands the QM part was terminated at Cβ with Cα replaced by a hydrogen link atom. The atomic charges of the QM region were fit with the RESP procedure from the electrostatic potential calculated at the B3LYP/lacvp/IEFPCM (ε = 4.0) level of theory with charges on the link H-atoms constrained to the sum of MM charges of atoms from a given residue that were left in the MM part of the system.[41] Ionization states of basic and acidic residues, atom types, and atomic charges of the MM part were the same as in MD simulations. The QM part has a neutral net charge, while the total charge of the whole model is −14.

Geometry optimizations for intermediates and transition structures were performed with the lacvp double-ζ basis set at the mechanical embedding level of approximation. During optimizations constraints were imposed on the residues from the MM region that are farther than 15 Å away from the active-site iron ion. Each stationary point was optimized in a two-step procedure. First, it was optimized with a set of atomic charges for the QM region determined in a previous optimization for a preceding stationary point. Second, a set of RESP atomic charges was determined for the obtained structure, and with this set the final optimization of a given stationary point was performed. The ONIOM energy of the optimized structure was computed at both the mechanical (ME) and electronic (EE) embedding levels with a triple-ζ basis set combining the cc-pVTZ(-f) basis for C, N, O, and H and the lacv3p+ basis and effective core potential for iron. The ONIOM energy was combined with a thermal correction to the Gibbs free energy computed at the ONIOM-ME(B3LYP/lacvp) level and the DFT-D2 dispersion correction computed for the QM region with the XYZ-Viewer program.[42,43] To test the stability of the results with respect to the choice of the functional, for some stationary points the electronic energies were also calculated using the B3LYP* functional, which has a smaller component of exact exchange (15% vs 20% for B3LYP).[44] DFT-D2 dispersion corrections and thermal corrections to the Gibbs free energy computed for the B3LYP models were added to B3LYP* electronic energies shown in Figure 7, below.

Stability of the results was also tested with respect to the choice of the QM part. To this end, the electronic energies were computed at the EE level with triple-ζ basis set for a high-level layer extended to 187 atoms and additionally including side chains of Phe190, Asn216, Phe311, Phe332, Phe337, and Leu340 with Cα replaced by a hydrogen link atom, two water molecules, and Pro214 with two carbonyl carbons of peptide bonds replaced by link atoms. Charges for the QM part were the same as in calculations for corresponding structures obtained with basic model (84 atoms in the QM part).

Kinetic isotope effects were computed on the basis of the semiclassical Eyring equation (eq 1) using differences between thermal

$$\mathrm{KIE} = \frac{{}^{\mathrm{H}}k}{{}^{\mathrm{D}}k} = \frac{e^{-{}^{\mathrm{H}}\Delta G^{\ddagger}/k_{\mathrm{B}}T}}{e^{-{}^{\mathrm{D}}\Delta G^{\ddagger}/k_{\mathrm{B}}T}} = \exp\left(\frac{{}^{\mathrm{D}}\Delta G^{\ddagger} - {}^{\mathrm{H}}\Delta G^{\ddagger}}{k_{\mathrm{B}}T}\right) \quad (1)$$

corrections to Gibbs free energies for each transition state with and without substitution by deuterium.

The AMBER force field was used to estimate the individual nonbonded (electrostatics and van der Waals) contributions for side chains of second-shell residues to the difference in energy between selected stationary points obtained with the QM/MM method. For this purpose, nonbonded interactions were computed with the AMBER force field for a full model of a given stationary point and a set of models where a single atom of a selected side chain had zeroed partial charge and van der Waals interaction parameter. From the difference, a contribution of a given atom was calculated. Sums of such atomic contributions over atoms constituting a given side chain were calculated for selected reactants and transition states, and their differences are used to infer about (de)stabilizing role of nonbonded interactions of a given residue for a selected process. The analysis of the role of selected residues from protein surrounding has been extended to pairwise classical interactions between the metal with its ligands and a given side chain, and these calculations were performed with the NAMD2 program[45] and the AMBER force field.

Abbreviations used in this contribution to label stationary points are the following: Int, intermediate; TS, transition state; SOSP, second-order saddle point.

Following is a summary of the other abbreviations used herein: HPPD, 4-hydroxyphenylpyruvate dioxygenase; HMS, hydroxymandelate synthase; HPP, 4-hydroxyphenylpyruvate; HG, homogentisate; HMA, (*S*)-hydroxymandelate; HPA, hydroxyphenylacetate; QM/MM, quantum mechanics/molecular mechanics; DFT, density functional theory; MD, molecular dynamics; KIE, kinetic isotope effect; WT, wild-type; RMSD, root-mean-square deviation.

3. RESULTS AND DISCUSSION

3.1. MD Simulations. Classical MD simulations were performed to model the structure of the HPPD-Fe(IV)═O-HPA complex. Since the HMS-Co(II)-HMA crystal structure (PDB code: 2R5V) is the only presently available source of detailed structural information on relevance to the HPPD-substrate/intermediate complexes, the starting geometry of HPA was transferred from the structure of HMS-Fe(IV)═O-HPA, which was obtained with MD simulations in our previous study.[9] During the MD simulation HPA adopted a distinctly different conformation in the HPPD substrate pocket than within the active site of HMS, which is consistent with different reaction specificities of the two enzymes (Figure 4).

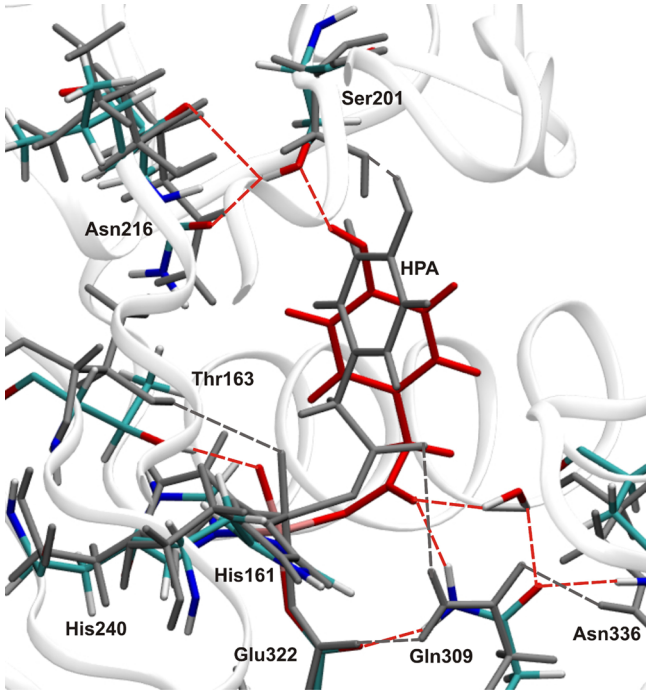

Figure 4. Representative snapshot from the MD simulation for the HPPD-Fe(IV)═O-HPA complex. HPA is shown in red, the starting structure in gray.

One can notice that the pro-S benzylic H-atom moved away from the oxo ligand and the substrate's ring approached the reactive Fe(IV)═O group. The OH group of HPA forms a H-bond with Ser201, which, in turn, H-bonds to Asn216. Such an arrangement of the HPPD-Fe(IV)═O-HPA active site is consistent with the QM/MM model suggested in a previous study.[23] Analogously to the HMS crystal structure, the carboxyl oxygen of HPA creates a H-bond to Gln309, and its distance oscillates around 2.00 Å during MD simulation. Interestingly, during the tenth ns of the simulation a water molecule entered

dx.doi.org/10.1021/ja506378u | J. Am. Chem. Soc. 2014, 136, 14472−14485

the active site and established H-bonds to the second carboxyl oxygen of HPA and the carbonyl oxygen of Gln309. Additional 10 ns of dynamics showed that this water molecule keeps these H-bonding interactions until the end of the simulation. As in HMS crystal structure Gln309 creates a H-bond also with Asn336, and its length oscillates around 2.00 Å. During the whole simulation, the hydroxyl group of HPA creates a H-bond with Ser201, which is involved in a H-bond with the carbonyl oxygen of Asn216. Analysis of the molecular dynamics trajectory showed that Thr163 forms a H-bond with the oxo ligand, whose length oscillates around 1.80 Å. Phe337 provides stacking interaction with the aromatic ring of HPA, which also has van der Waals contacts with Phe332 and Phe190. To test the stability of the obtained model of the HPPD-Fe(IV)═O-HPA complex, 10 snapshots were selected (after 15, 16, 17, 18, 19, 20, 21, 22, 23, and 24 ns of MD simulation), minimized, and superimposed. The RMSD of these structures calculated with respect to the average geometry is within 0.74 Å for the backbone atoms and 1.28 Å for all atoms, which together with preservation of the most important H-bonding contacts in the active site and the HPA orientation indicates that the core of the complex remains in the minimum reached during the MD simulation (Supporting Information, Figure S4).

The RMSD, computed for the backbone atoms with respect to the starting geometry, reached a plateau at a value of 1.8 Å after 12 ns of simulations (Figure S1). Atomic fluctuations computed for the 14th ns of the simulated trajectory (Figure S2) reveal that in the vicinity of the active site the structure fluctuates moderately and remains in the same basin of attraction. The most mobile fragments of the protein are loops that are distant from the active site (Figures S2 and S3).

3.2. QM/MM Studies. In this study several reaction channels for decay of the ferryl species (R, Figure 5) were considered (see Figure 6), including attack at the C1, C2, or C6 carbons of HPA and direct formation of the epoxide intermediate across C1−C2 or C1−C6 bonds. For the subsequent steps, formation of the epoxide from the radical σ-complex (Int1) and 1,2-acyl migration from the C1 to C2 or C6 position in the ring were taken into account. All reactions were modeled for the quintet spin state consistently with the results of the previous studies.[8,14,24]

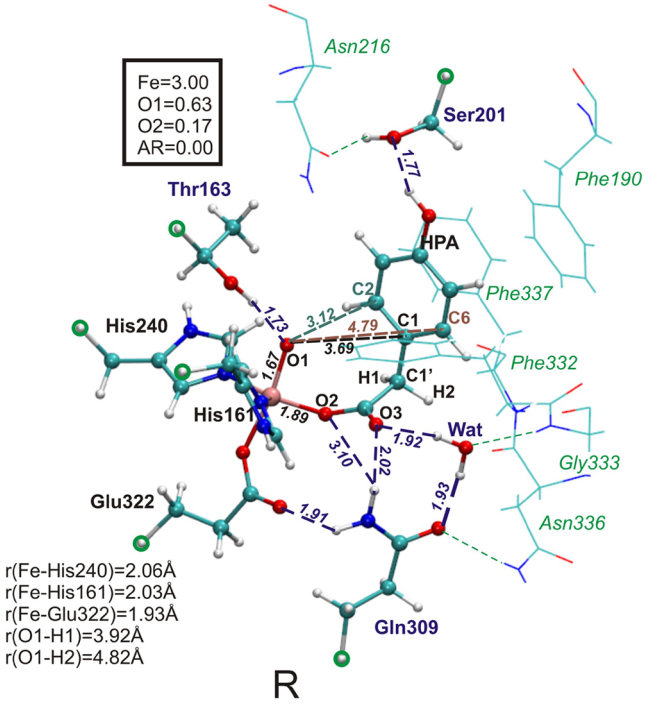

Figure 5. Active-site region of the macromolecular R complex optimized with the ONIOM method. QM part in ball-and-stick representation. Hydrogen link atoms are marked with green circles. Relevant atomic spin populations are shown in the frame.

3.2.1. Electrophilic Attack on the Aromatic Ring of HPA. (a). Electrophilic Attack at the C1 Ring Position. The activation energy connected with the attack of the oxoferryl group at the C1 position (TS1) amounts to 18.0 kcal/mol, which, taking into account differences in models and methods, compares rather well with the barrier computed previously on the DFT level: for electrophilic attack of the Fe(IV)═O species on the benzene in heme enzymes, the barrier is 17.5 kcal/mol (for low-spin state) and 20.6 kcal/mol (for high-spin state),[46] for the α-ketoglutarate biomimetic system it is 14.9 kcal/mol,[47] and for phenylalanine hydroxylase it is 16.2 kcal/mol;[48] and previous studies on minimal models of HPPD reported 16.9 kcal/mol[8] and 16 kcal/mol.[14] The resulting radical σ-complex intermediate (Int1) lies 3.5 kcal/mol above the oxoferryl complex (Figure 7). The QM region of the optimized TS1 is presented in Figure 8. In this transition structure the distance between the oxo ligand (O1) and the C1 carbon is 2.06 Å, whereas the Fe−O1 distance is elongated to 1.82 Å from 1.67 Å in R.

TS1 leads to a radical σ-complex (Int1) featuring a high-spin Fe(III) and an antiferromegnetically coupled π-radical on the ring, which agrees with the results of previous QM studies.[8,9,14]

(b). Alternative Attacks at the C2 and C6 Ring Positions. The alternative electrophilic attack at the C2 carbon (green line, TS4 and Int2′, see Figure 7) involves a barrier of 26.8 kcal/mol, which is significantly higher than for the attack at the C1 position (18 kcal/mol). In the QM region of TS4, the critical O1−C2 and Fe−O1 distances are 1.89 and 1.82 Å, respectively. The MM region of the TS4 structure is very similar to that in TS1 with the exception of a significantly different orientation of Phe332, which in TS4 is too far away from HPA to effectively interact with its aromatic ring. Accordingly, nonbonding interactions of Phe332 destabilize TS4 with respect to R by 0.79 kcal/mol (see Table 1). Such a nonoptimal orientation of HPA also weakens stacking interaction between the HPA aromatic ring and Phe337 (+0.49 kcal/mol, Table 1) and other dispersion interactions with Phe190 (+0.82 kcal/mol, Table 1). These weakened van der Waals interactions between HPA and residues from the local environment of the protein, together with slightly weaker Ser201-HPA (1.80 vs 1.77 Å in R) and considerably weaker Ser201-Asn216 (1.97 Å vs 1.83 Å) H-bonds, contribute to the high barrier connected with TS4 and the high energy of the resulting radical σ-complex Int2′ (see Figure 7). The directing effect of the OH-substituent also disfavors electrophilic attack at C2 and C6.

A transition structure (TS5) for attack at the C6 carbon was found to have even higher energy than TS4, i.e., 41.4 vs 26.8 kcal/mol. In TS5, the aromatic ring of HPA loses van der Waals contacts with Phe332 and Phe337, and the H-bond between Ser201 and Asn216 is very elongated (H−O distance of 2.40 Å in comparison to 1.84 Å in TS1). These structural differences explain the large energy gap between TS5 and TS1.

3.2.2. Migration of the Acetic Acid Substituent. The 1,2-migration of the carboxymethyl substituent is the next reaction step taking place after the electrophilic attack on the aromatic ring of HPA. With the model and method employed here, only

dx.doi.org/10.1021/ja506378u | J. Am. Chem. Soc. 2014, 136, 14472−14485

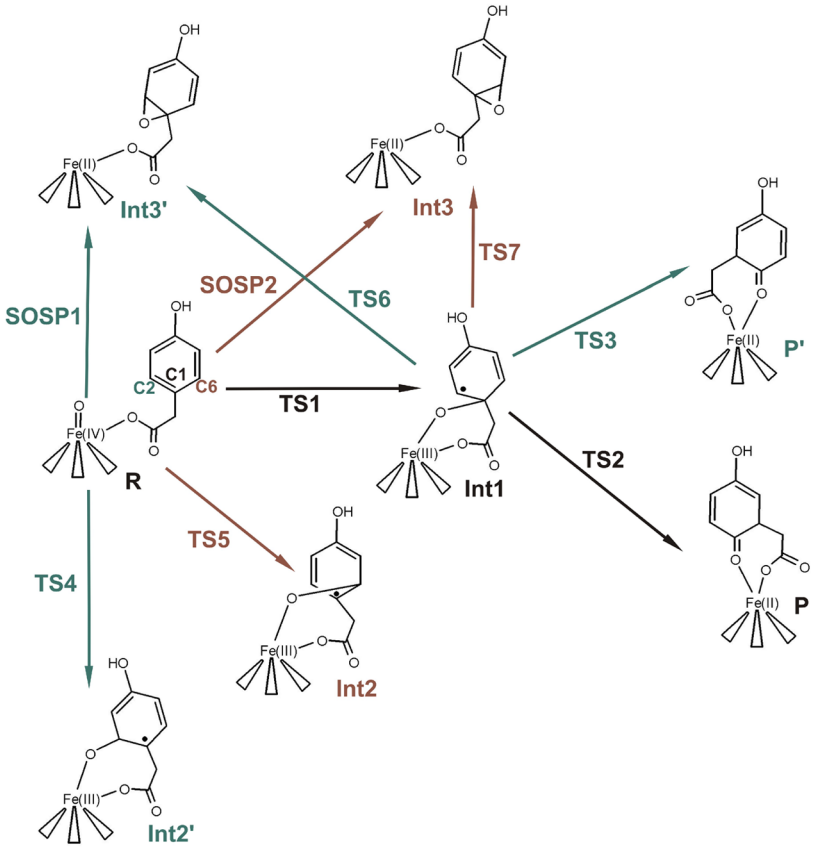

Figure 6. Reaction channels considered in this work: brown, reaction steps involving the C6 carbon; green, reaction steps involving the C2 carbon.

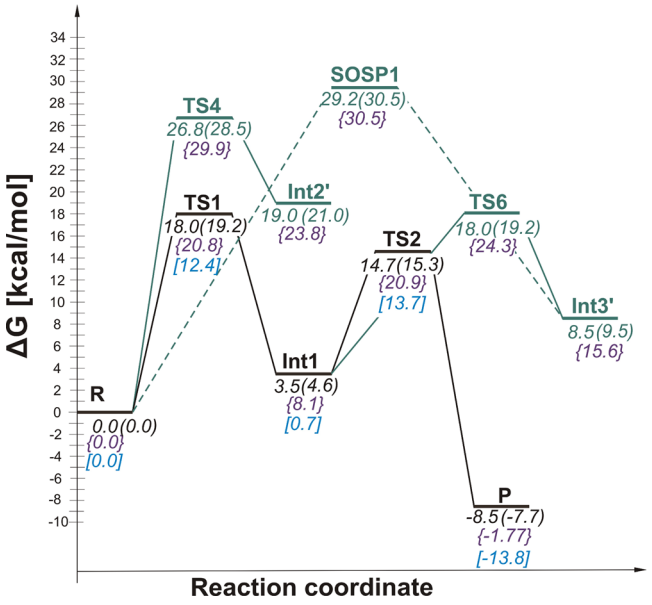

Figure 7. Reaction free energy profiles, computed at the B3LYP/triple-ζ ONIOM-EE level for steps involving the C1 and/or C2 carbons: in green, reaction steps involving C2; in black, the lowest energy path. The values in parentheses are the relative free energies calculated with the B3LYP/triple-ζ ONIOM-ME energy. Relative ONIOM-EE free energies for the model lacking the second-shell water are shown in square brackets in blue; free energies computed with the B3LYP*/triple-ζ ONIOM-EE electronic energy values are shown in curly brackets in violet.

the heterolytic reaction channel proceeding as a single-step reaction could be found for this process. All attempts to find a transition state and intermediate of the alternative homolytic mechanism have been unsuccessful.

Two possible directions of the migration were considered (Figure 6), i.e., from C1 to C6 (Int1→P) and from C1 to C2 (Int1→P′). The Int1→P reaction was found to involve a barrier of 11.2 kcal/mol (TS2), whereas for the alternative Int1→P′ direction the computed barrier is somewhat higher, i.e., 14.5 kcal/mol.

The active-site regions of TS2 and P are shown in Figure 9. In TS2, the length of the bond being broken, i.e., C1′−C1, is 2.16 Å, whereas the distance between carbons forming a new bond, i.e., C1′−C6, is 2.32 Å. The imaginary frequency of TS2 (see Supporting Information) clearly displays a movement of the substituent from C1 to C2, cleavage of the C1−C1′ bond, and formation of the C6−C1′ bond. Comparison of spin populations for Int1 (Figure 8) and TS2 (Figure 9) reveals that between these two stationary points an electron transfer takes place from the substrate's ring to the metal ion, and thus, formally the migration occurs for the ring carbocation. Such an electron transfer is facilitated by the presence of H-bonds between the first and the second-shell ligands, whose strength is expected to increase as the Lewis acidity of iron drops upon Fe(III)-to-Fe(II) reduction. As shown in Figure 8 and 9, we observe considerable contraction of H-bonds formed by Ser201 and Thr163 when going from Int1 to TS2.

For our previous computational study of HPPD, no structural data were available that defined the HPA binding mode, hence the QM model used at that time did not included any of the second-shell residues. This shortcoming, in turn, stabilized the radical path at the expense of the heterolytic pathway that was found most likely in the present work.

dx.doi.org/10.1021/ja506378u | J. Am. Chem. Soc. 2014, 136, 14472−14485

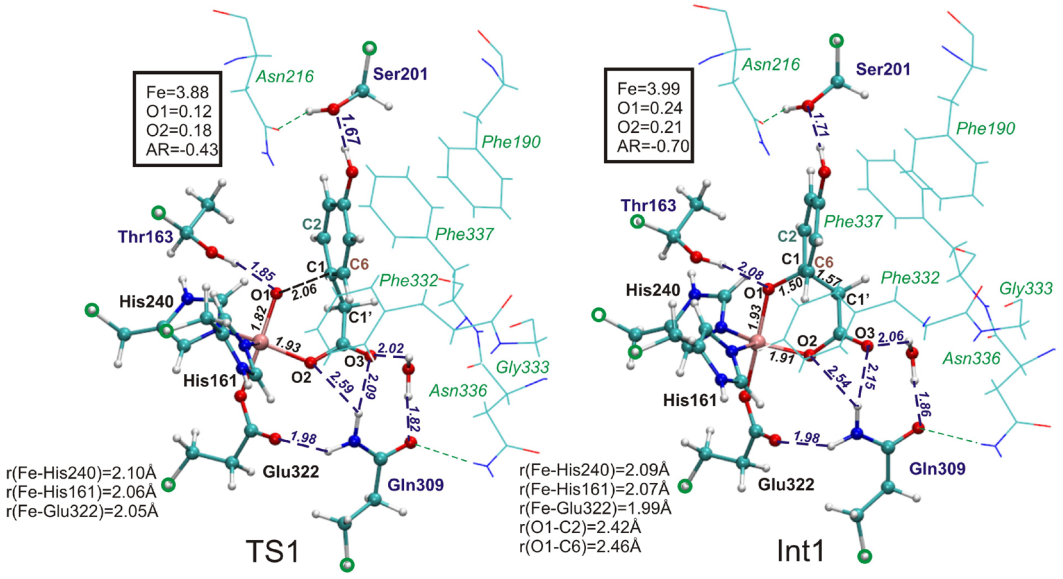

Figure 8. Active-site regions of the optimized structures of TS1 for the electrophilic attack at the C1 position in the HPA aromatic ring and for the radical σ-complex intermediate Int1. QM part in ball-and-stick representation. Hydrogen link atoms are marked with green circles. Relevant atomic spin populations are given in frames.

Table 1. Relative Classical Nonbonded Contributions (in kcal/mol) to the Activation Energies for Electrophilic Attack on the C1 Carbon (R→TS1) and the Pro-S Benzylic Hydrogen Atom Abstraction (R→TS8)[a]

residue HPPD/HMS	TS1 for attack on C1: HPPD/HMS	TS8 for pro-S H-atom abstraction: HPPD/HMS	TS4 for attack on C2: HPPD
Thr163/−	−2.42 (−1.93)/−	−0.01 (−0.90)/−	−1.80
Phe190/−	+0.10 (+0.56)/−	−0.13 (+0.17)/ −	+0.82
Ser201/Ser201	−0.34 (−1.71)/−0.94	−0.39 (−0.56)/+0.16	+0.91
Ala203/Val203	+0.18 (−0.11)/+0.85	+0.35 (−0.27)/+0.64	+0.22
Pro214/Thr214	+2.57 (+0.90)/+2.57	+0.61 (−0.46)/+1.65	−0.01
Asn216/Ile216	+0.21 (−0.36)/+0.60	+0.17 (+0.39)/+0.20	+5.29
Gln309/Gln305	−3.76 (−1.24)/+0.16	−2.13 (+0.08)/+0.29	−0.80
Phe332/Phe330	+0.54 (−0.78)/+1.04	+1.37 (+0.85)/−0.03	+0.79
Asn336/Asn334	+0.69 (−1.50)/+0.20	+0.33 (−0.63)/+0.91	−0.15
Phe337/Ile335	+0.17 (+0.74)/+0.49	+1.26 (+1.39)/−0.50	+0.49
WAT/−	+5.49 (+1.66)/−	+5.15 (+1.50)/−	+0.09

[a]For comparison, results obtained in the previous study on HMS are also given.[9] In parentheses are contributions from pairwise classical interactions between the metal cofactor with its ligands and a given side chain in each transition state (computed with the NAMD2 program).

The transition state (TS3) and the ketone product P′ for the alternative C1−C2 migration were also found (Figure S8), yet the barrier is by 4.2 kcal/mol higher than for the preferred Int1→TS2→P pathway. This process is coupled to a significant rotation of the HPA aromatic ring around the O1−C1 bond.

3.2.3. Formation of the Epoxide Intermediate. (a). Direct Formation of Epoxide from Oxoferryl Intermediate. Consistent with the results of the previous DFT studies,[8,49,50] it was found that the stationary points directly connecting the oxoferryl intermediate (R) with the epoxide intermediates (Int3 or Int3′) are characterized by two imaginary frequencies; i.e., they are second order saddle points (SOSPs). The normal mode connected with one imaginary frequency describes a symmetrical insertion of the O-atom into the aromatic ring, and the second one represents an antisymmetrical distortion toward transition structures for the electrophilic attack on one of the two carbons (for animations see .pdb files in the Supporting Information). This happens also for heme enzymes.[46,51]

Moreover, the computed free energies of SOSP1 (29.2 kcal/mol, Figure 7) and SOSP2 (34.7 kcal/mol) are considerably higher than the activation energy connected with TS1 (18.0 kcal/mol).

In SOSP1 the Fe−O1 bond is elongated to 2.01 from 1.67 Å, whereas the O1−C1 and O1−C2 distances are rather short, i.e., 2.02 and 1.85 Å, respectively (Figure 10). Concerning the electronic structure of SOSP1, a gross spin population of −0.19 on the substrate's aromatic ring indicates substantial spin polarization is present during such an O-atom insertion. This spin polarization is a physical reason why the symmetrical O-atom insertion proceeds via a SOSP rather than along a true reaction coordinate with a transition state.

The reason why the direct insertion of oxygen (from Fe(IV)═O) across the C1−C2 bond is not viable, can be traced in the electronic structure changes along such a "reaction" coordinate. For this purpose it is instructive first to analyze a prototypical reaction, symmetrical insertion of an O-atom species into ethylene (Figure 11). Orbitals active in this process are the following: two oxygen 2p orbitals, one parallel

dx.doi.org/10.1021/ja506378u | J. Am. Chem. Soc. 2014, 136, 14472−14485

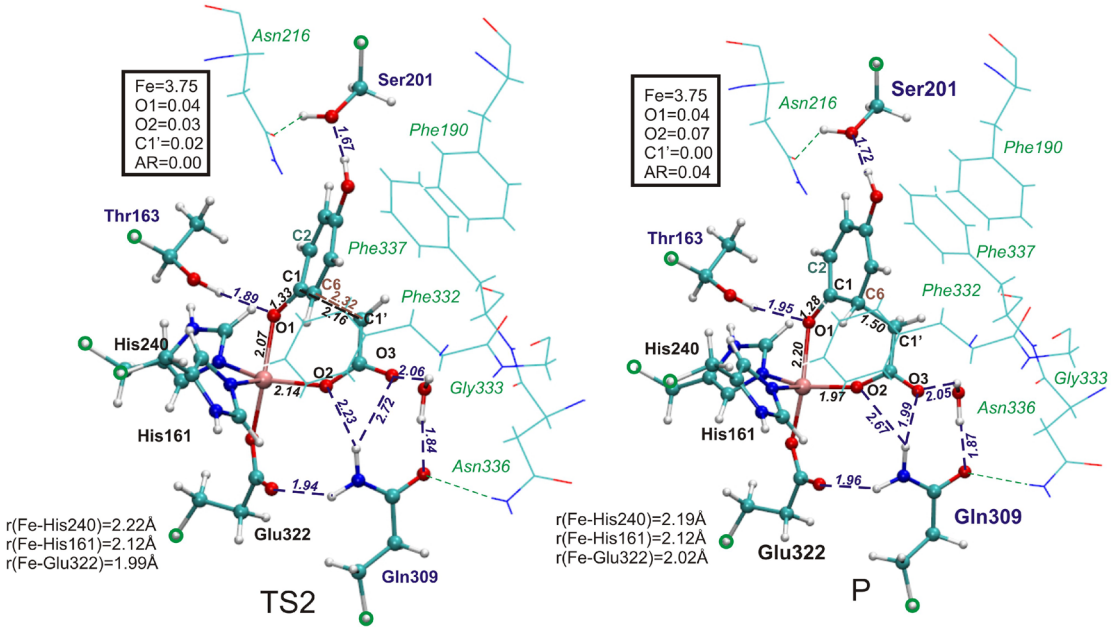

Figure 9. Active-site regions from the optimized structures of the transition structures: TS2 for the C1−C6 migration of carboxymethyl side chain and the ketone intermediate P. QM part in ball-and-stick representation. Hydrogen link atoms are marked with green circles. Relevant atomic spin populations are reported in frames.

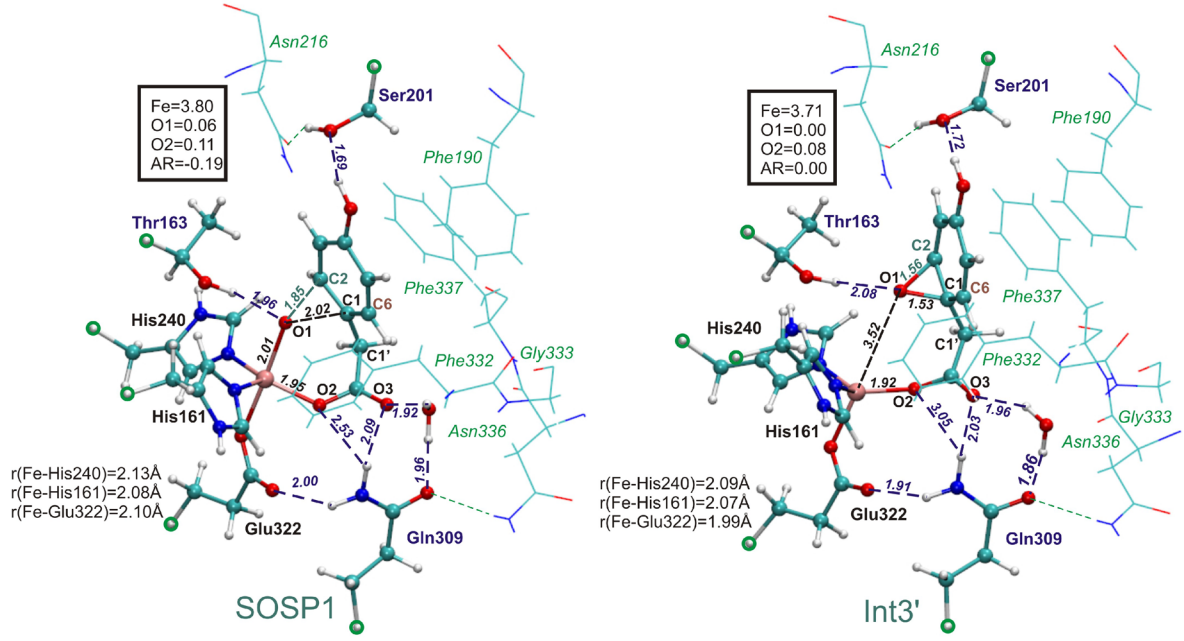

Figure 10. Active-site regions from the optimized structures of the second order saddle point SOSP1 for direct formation of the C1−O1−C2 epoxide intermediate, and the epoxide intermediate Int3′. QM part in ball-and-stick representation. Hydrogen link atoms are marked with green circles. Relevant atomic spin populations are reported in frames.

to the C−C bond (O p_A) and one pointing toward the midpoint of the C−C bond (O p_S), and two π orbitals of ethylene (π_S, π_A^*). The third oxygen 2p orbital is perpendicular to the C−C bond and the direction of attack, and in the epoxide product it becomes an oxygen lone pair. Assuming the C_s symmetry, these active orbitals can be classified as either symmetric (S) or antisymmetric (A) with respect to the reflection in the symmetry plane (perpendicular to the C−C bond and passing through oxygen and the midpoint of the C−C bond), and hence their subscripts. The resulting bonding and antibonding orbitals of the epoxide are shown in Figure 11A.

With the simple orbital correlation diagram, as in Figure 11B, we can analyze when the process should be energetically favorable or not. First, we take the case of an O-atom in an open-shell singlet state (Figure 11C). From the correlation diagram we see that in this case we obtain the epoxide in an excited singlet state, and hence, such a process in not symmetry-allowed. However, if the oxygen electrons are paired (closed-shell singlet, Figure 11D), the reaction yields the epoxide in the ground state; i.e., the process is symmetry-allowed. With one more electrons on oxygen (oxygen radical anion, Figure 11E) we would obtain an epoxide anion with the unpaired electron on the W_S^* orbital.

dx.doi.org/10.1021/ja506378u | J. Am. Chem. Soc. 2014, 136, 14472−14485

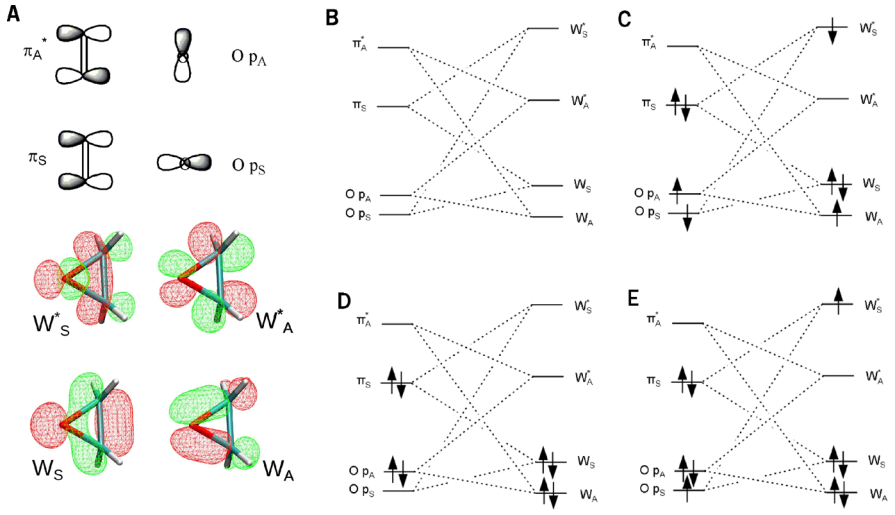

Figure 11. Orbitals and orbital correlation diagrams for symmetrical (Cs) insertion of an oxygen species into ethylene: (A) cartoon and contours of active orbitals, (B) orbital correlation diagram, (C) diagram for insertion of the O-atom in an open-shell singlet state, (D) diagram for insertion of the O-atom in a closed-shell singlet state, and (E) diagram for insertion of $O^{-\bullet}$.

However, such a system is not stable, and when allowed to relax with no symmetry constraints it converts to a species with one of the C−O bonds broken.

From the above analysis it follows that we could expect that a symmetrical oxygen insertion across a double C−C bond should be possible only when the symmetrical oxygen 2p orbital (O p_S), which is the first one to overlap with the C=C π_S orbital, could be easily depleted of two electrons. This is possible for a heterolytic cleavage of an O−O(H) bond, as for example found for naphthalene dioxygenase (see Figure 12A).[52]

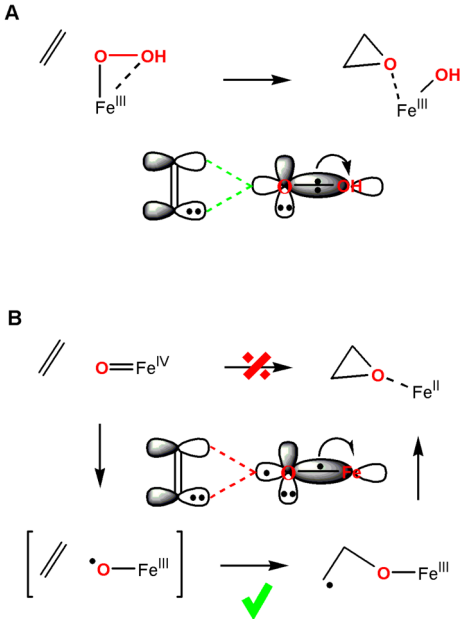

Figure 12. Reaction cartoons for (A) symmetrical O-insertion by a HOO-Fe(III) species, as in NDO,[52] and (B) asymmetrical attack by the high-spin ferryl species.

However, as argued below, this is not the case for a high-spin Fe(IV)=O species. An analysis of the natural orbitals and natural spin orbitals calculated for SOSP1 (see Figures S11 and S12) revealed that at this stage of the "reaction" an alpha electron has already been transferred to the metal ion from the oxo ligand/ring and the beta electron is being shifted. Thus, the electronic structure of SOSP1 can be graphically represented by a schematic cartoon shown in Figure 12B, where we can notice the unfavorable three-electron interaction between O p_S and the π_S of the ring. Thus, due to exchange interactions on the high-spin iron ion the transfer of the two electrons is decoupled with the alpha (majority spin) electron being transferred first and the beta electron lingering behind. This spin polarization implies that around the midpoint of the "reaction" the electronic structure is close to that expected for Fe(III)-$O^{-\bullet}$ attacking a double bond, and for such a species the preferred reaction channel is the asymmetric radical attack on one of the C-atoms (Figure 12B).

Previous theoretical studies devoted to hydroxylation of aromatic ring by heme enzymes also ruled out direct epoxidation of benzene in favor of the formation of radical or cationic σ-complexes.[46,50] Instead, stepwise mechanism of epoxidation, including formation of σ-complex and further ring closure reaction, had been previously suggested by Kumar et al. and backed with electronic structure arguments based on the valence bond theory.[49]

(b). Formation of Epoxide from the Radical σ-Complex. The epoxide intermediate might form via closing the epoxide ring in the radical σ-complex (Int1), and two channels, leading to Int3′ or Int3, were considered (for transition structures see Figure S10).

TS6 leads from Int1 to the C1−O1−C2 epoxide Int3′, and its relative free energy amounts to 18.0 kcal/mol, i.e., 3.3 kcal/mol higher than for TS2. Formation of the epoxide is not only kinetically unfavorable, but also so from the thermodynamic standpoint. In Figure 7, one can notice that closing the ring (Int1→Int3′) is an endergonic process (+5.0 kcal/mol), whereas the migration (Int1→P) is substantially exergonic (−12.0 kcal/mol). In TS6 the C1−O1 and O1−C2 distances are 1.51 and 1.82 Å, respectively, while the Fe−O1 bond is significantly elongated, from 1.93 Å in Int1 to 2.59 Å. The formation of the C1−O1−C6 epoxide via TS7 is connected with the activation free energy by 1.4 kcal/mol higher than for the C1−O1−C2 counterpart.

Taken together, the results presented above show that the energetically preferred mechanism of the HPPD catalytic

dx.doi.org/10.1021/ja506378u | J. Am. Chem. Soc. 2014, 136, 14472−14485

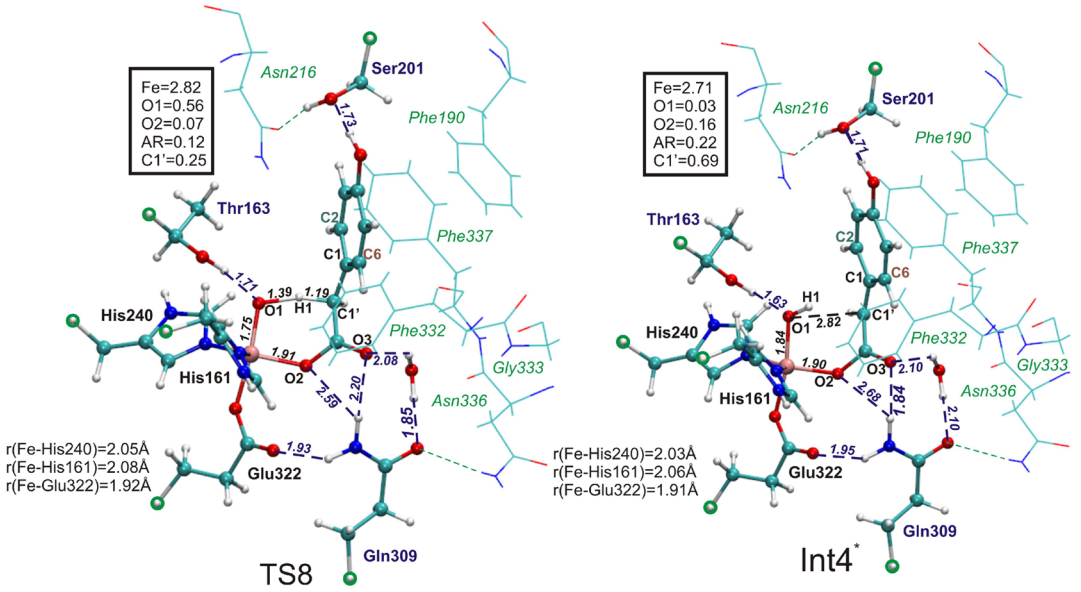

Figure 13. Active-site regions from optimized structures of the transition structure for the pro-S hydrogen atom abstraction (TS8) and the benzylic radical intermediate in an excited state (Int4*). QM part in ball-and-stick representation. Hydrogen link atoms marked with green circles. Relevant atomic spin populations are reported in frames.

reaction proceeds through an electrophilic attack of the Fe(IV)-oxo at the C1 aromatic carbon (R→TS1), which yields the radical σ-complex/Fe(III) (Int1; Figure 6). In the subsequent step, the carboxymethyl substituent migrates in a single-step heterolytic rearrangement process (Int1→TS2→P). The C6 position of the HPA ring is the preferred destination site for the migration.

3.2.4. Variations of the QM/MM Models and Methods. The key stationary points along the main reaction coordinate were also optimized for a model lacking the second-shell water molecule (Figure 7; for structures see the Supporting Information). From the energy profile one can notice that removing the water lowers the relative energies with respect to R, which is a consequence of the fact that only for R the water can form a H-bond with the backbone hydrogen of Gly333 (Figure 5), for other species there is not enough room between the carboxyl group of the substrate and Gly333 to accommodate a water molecule. The two barriers along the suggested reaction coordinate, connected with TS1 and TS2, are affected to a different extent, and in the model lacking the water molecule the second barrier becomes higher than the first one, which would help to expose KIE connected with this step in the overall measured value. To test the stability of the results with respect to the size of QM part, the electronic energies, at the B3LYP/triple-ζ ONIOM-EE level, were also computed for the model with the QM system extended from 84 to 187 atoms, including additionally side chains of Phe190, Pro214, Asn216, Phe311, Phe332, Phe337, Leu340, and two water molecules. Results of these computations show (Figure S6) that moving another layer of residues from the MM to the QM part of the system noticeably decreases activation energies. The electronic energies of stationary points obtained with the basic model were also computed at the B3LYP*/triple-ζ ONIOM-EE level. Most importantly, the reaction energy profiles obtained with the B3LYP and B3LYP* functionals (Figures 7 and S6) lead to the same qualitative conclusions with respect to the preferred reaction channel for the HPPD reaction, running from R through TS1→Int1→TS2→P. QM/MM free energy calculations will be a logical next step of the studies on the reaction catalyzed by HPPD, as they are expected to provide more accurate free energy reaction profiles.[53]

3.2.5. Benzylic Hydrogen Atom Abstraction. Since the catalytic reaction of HMS involves benzylic hydroxylation, and HMS and HPPD are closely related (*vide supra*), it was interesting to test if such a reaction is energetically viable within the active site of HPPD. The C1′−H cleavage reaction was studied for both benzylic H-atoms, i.e., the pro-S and the pro-R hydrogens. Abstraction of the pro-S hydrogen (H1) (Figure 13) involves a barrier of 24.9 kcal/mol (24.6 kcal/mol with B3LYP*; TS8), while for the pro-R one it is 27.6 kcal/mol (TS9). The pro-R hydrogen is more difficult to access by the oxo ligand because along this reaction coordinate the H-bond between the Ser201 side chain and the hydroxyl group of HPA needs to be ruptured.

In agreement with the results of previous studies on the HMS reaction,[8,9,14] the C−H cleavage leads to an intermediate with a benzylic radical and a ferric ion in an intermediate spin state. The activation barrier for cleavage of the pro-S H−C1′ bond (TS8) is by 6.9 kcal/mol higher than for the electrophilic attack on the ring (TS1), which means that the present macromolecular model successfully reproduces the regiospecificity of the catalytic reaction of HPPD. In order to get some qualitative insight into the origin of this 6.9 kcal/mol difference between the barriers connected with TS1 and TS8 computed at the B3LYP/triple-ζ ONIOM-EE level, contributions to the classical nonbonding interaction energies (van der Waals and electrostatics, calculated with the AMBER force field) from the side chains of the second-shell residues were computed for TS1, TS8, and R geometries and compared (see Table 1). It should be mentioned that in case of HMS[9] that analysis was done for a cluster QM model.

Analyzing nonbonded contributions, among all residues selected, Thr163, Gln309, Ala203, Phe332, and Phe337 stabilize TS1 with respect to TS8, whereas Pro214, Asn336, Phe190, Ser201, Asn216, and a water molecule work in the opposite direction. These results indicate that selected residues

dx.doi.org/10.1021/ja506378u | J. Am. Chem. Soc. 2014, 136, 14472−14485

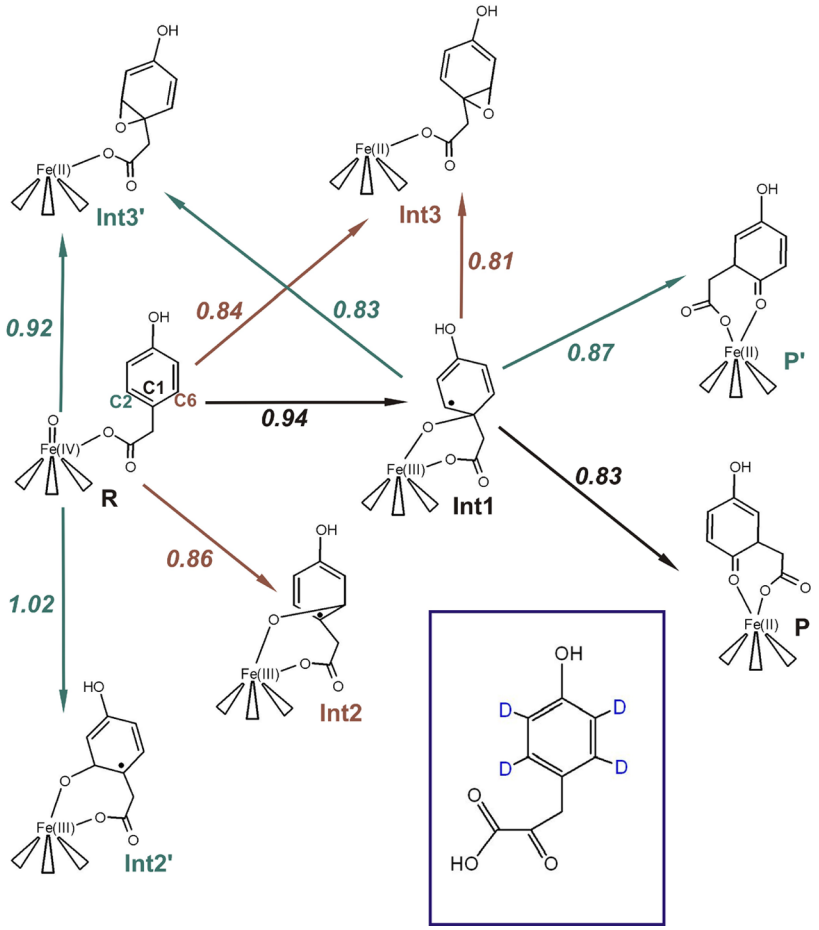

Figure 14. KIE values computed for ring deuterio-HPP.

contribute to the regioselectivity of HPPD/HMS reactions. Pairwise interactions between the first-shell metal ligands and the second-shell residues were also calculated (Table 1). Taking into account only the pairwise interactions, Thr163, Ser201, Asn216, Gln309, Phe332, Asn336, and Phe337 stabilize TS1 with respect to TS8, while Phe190, Ala203, Pro214, and a water molecule destabilize it. Thus, direct interactions between Ser201, Asn216, Asn336, and a metal cofactor with its ligands stabilize TS1 vs TS8, but when their interactions with other residues are included, they provide a destabilizing contributions. Notably, the destabilizing effect of a water molecule to the overall energy of TS1 equals to 5.49 kcal/mol, which is very close to the difference in energies of TS1 obtained with the models differing in presence/absence of this water (5.6 kcal/mol, Figure 7). The largest stabilizing contribution to the energy of TS1 with respect to TS8 is provided by Thr163 (2.41 kcal/mol), but the largest direct stabilizing effect (from pairwise interactions) comes from Phe332 (1.6 kcal/mol). Nonbonded interactions of Phe332 favor TS1 over TS8 by 0.8 kcal/mol. However, in HMS a phenylalanine (Phe330) placed in this position contributes −1.0 kcal/mol to the difference between the barriers.[9] Both residues, i.e., Phe332 and Phe330, are conserved in HMS and HPPD, respectively, which shows that differences in shape of the active sites of HMS and HPPD together with the different steric requirements of the reaction coordinates cause that the same residues in the same positions can favor two different reactions, in each case the native reaction of a given enzyme. Asn216 provides slightly destabilizing contribution to the energy of TS1 with respect to TS8. In line with the results of the mutagenesis studies,[15] in HPPD Phe337 favors TS1 to TS8, whereas in HMS Ile216 and Ile335 favor the transition state for H-atom abstraction (Table 1). Thr163 in HPPD and Thr214 in HMS, which form H-bond to the oxo ligand of the ferryl species, significantly favor the TS:s of the native reactions of these enzymes. Asn216 of HPPD is predicted not to contribute significantly to the difference in the barrier heights, whereas mutagenesis studies reflect its role as HPPD double mutants including Asn216 shows HMS activity. However, as it may be noticed in Table 1, its presence significantly disfavors an electrophilic attack on the adjacent carbon in the ring. Pairwise interactions between Asn216 and the metal ion with its ligands stabilize TS1 vs TS8 by 0.8 kcal/mol, which confirms the role of this residue in arranging the local structure of the active site.

3.2.6. Computations of KIE. In an experimental work using a ring deuterated HPA, a KIE value of 0.84 was measured for WT HPPD.[17] In accordance, KIE values computed in this work (see Figure 14) for the two steps of the energetically preferred pathway are also smaller than one; i.e., for the electrophilic attack at the C1 carbon of the ring (TS1), KIE = 0.94, and for the C1−C6 migration (TS2), KIE = 0.83.

Interestingly, in additional computations done with the B3LYP* functional the order of activation energies connected with TS1 (20.8 kcal/mol with respect to R) and TS2 (20.9 kcal/mol with respect to R) is reversed; i.e., TS2 has a little higher free energy. Thus, it appears likely that the substituent migration, with its computed KIE of 0.83, is the rate-limiting step for the decay of the ferryl species, which might give a good agreement between the calculated and the experimentally determined (0.84) values of KIE.

dx.doi.org/10.1021/ja506378u | J. Am. Chem. Soc. 2014, 136, 14472−14485

Since the inverse KIE is typically interpreted in the context of sp^2-to-sp^3 hybridization changes, improper dihedral angles, which are a measure of planarity of the critical carbon atom (C6), were measured for TS2 and SOSP1 and amount to 172.2° and 148.8°, respectively. Thus, larger deviation from planarity observed for SOSP1 (KIE = 0.92) does not result in a larger KIE value. Clearly, some other factors are in play, and we propose that the relatively large inverse KIE effect calculated for TS2 is rooted in the change of oxidation state of the ring of the substrate taking place in this reaction step. Indeed, a KIE effect for ionization of a ring radical computed for a simplified model of Int1 is notably inverse with a value of 0.81 (see Supporting Information).

The KIE value was also computed for 1′,1′-dideuterio substrate, for which an experimental value of 0.99 has been reported[27] for WT and 1.39 for N216S mutant. For this substrate and the Int1→TS2 step the calculated KIE value amounts to 1.26, which falls roughly in the middle between the two measured values.

4. CONCLUSIONS

The ONIOM model adopted in this work, with the QM part including all polar residues lining up the substrate pocket, allowed us to study the HPPD hydroxylation and rearrangement reactions with the protein steric and electrostatic effects included in the model. With this approach we not only successfully reproduced the observed reaction specificity (benzylic hydroxylation, which is typical for HMS, has a significantly higher barrier by 6.9 kcal/mol), but also managed to arrive at a mechanism that is consistent with available KIE data. The observed inverse KIE effect was attributed to ring oxidation accompanying the substituent migration. Classical nonbonded interactions of second-shell residues were analyzed for R and the two TSs decisive for product specificity, identifying key residues mostly affecting the direction of the catalytic reaction. Concerning the reaction mechanism itself, the new finding of this study is that irrespective of the radical character of the σ-complex intermediate (INT1), the rearrangement is a single step heterolytic process, with a ring-to-iron electron transfer taking place early on the reaction coordinate. The previously proposed formation of the putative epoxide intermediate directly from the ferryl species was found not to be viable both because of a high "activation" energy and also on the grounds of the electronic structure analysis, which helped to explain why this "reaction coordinate" involves a second-order saddle point rather than a transition state.

■ ASSOCIATED CONTENT

Supporting Information

Figures S1−S15, presenting QM regions of geometry optimized species not shown in the main text and natural orbitals computed for ^{5}SOSP1; table listing contributions to ONIOM extrapolated energies computed for each stationary point; PDB files with coordinates of stationary points found with the ONIOM method, B3LYP/triple-ζ ONIOM-EE energies calculated for the model with QM part extended from 84 to 187 atoms, and electronic energies computed at the B3LYP*/triple-ζ ONIOM-EE level of theory. This material is available free of charge via the Internet at http://pubs.acs.org.

■ AUTHOR INFORMATION

Corresponding Author

ncborows@cyf-kr.edu.pl

Notes

The authors declare no competing financial interest.

■ ACKNOWLEDGMENTS

"Kraków Interdisciplinary PhD-Project in Nanoscience and Advanced Nanostructures" is operated within the Foundation for Polish Science MPD Programme, co-financed by the EU European Regional Development Fund. This research project was supported by grants no. DEC-2011/01/N/ST4/02330 (A.W.) and no. UMO-2011/01/B/ST4/02620 (T.B., E.B.) from the National Science Centre, Poland. This research was supported in part by PL-Grid Infrastructure. We are grateful to Sven de Marothy for providing us with his XYZ-Viewer program.

■ REFERENCES

(1) Knox, W. E.; Edwards, S. *Methods Enzymol.* **1955**, *2*, 287−300.
(2) Lindblad, B.; Lindstedt, G.; Lindstedt, S.; Rundgren, M. *J. Biol. Chem.* **1977**, *252*, 5073−5084.
(3) Moran, G. R. *Arch. Biochem. Biophys.* **2005**, *433*, 117−128.
(4) Goodwin, T. W.; Mercer, E. I. *Introduction to Plant Biochemistry*; Pergamon Press: Sydney, 1983.
(5) Choroba, O. W.; Williams, D. H.; Spencer, J. B. *J. Am. Chem. Soc.* **2000**, *122*, 5389−5390.
(6) Hubbard, B. K.; Thomas, M. G.; Walsh, C. T. *Chem. Biol.* **2000**, *7*, 931−942.
(7) Brownlee, J.; He, P.; Moran, G. R.; Harrisson, D. H. T. *Biochemistry* **2008**, *47*, 2002−2013.
(8) Borowski, T.; Bassan, A.; Siegbahn, P. E. M. *Biochemistry* **2004**, *43*, 12331−12342.
(9) Wójcik, A.; Broclawik, E.; Siegbahn, P. E. M.; Borowski, T. *Biochemistry* **2012**, *51*, 9570−9580.
(10) Pratter, S. M.; Konstantinovics, C.; Giuro, C. M. L. D.; Leitner, E.; Kumar, D.; de Visser, S. P.; Grogan, G.; Straganz, G. D. *Angew. Chem.* **2013**, *125*, 9859−9863.
(11) Brownlee, J.; Johnson-Winters, K.; Harrison, D.; Moran, G. *Biochemistry* **2004**, *43*, 6370−6377.
(12) Yang, C.; Pflugrath, J. W.; Camper, D. L.; Foster, M. L.; Pernich, D. J.; Walsh, T. A. *Biochemistry* **2004**, *43*, 10414−10423.
(13) Serre, L.; Sailland, A.; Sy, D.; Boudec, P.; Rolland, A.; Pebay-Peyroula, E.; Cohen-Addad, C. *Structure* **1999**, *7*, 977−988.
(14) Neidig, M.; Decker, A.; Choroba, O.; Huang, F.; Kavana, M.; Moran, G.; Spencer, J.; Solomon, E. *Proc. Natl. Acad. Sci. U.S.A.* **2006**, *103*, 12966−12973.
(15) O'Hare, H.; Huang, F.; Holding, A.; Choroba, O.; Spencer, J. *FEBS Lett.* **2006**, *580*, 3445−3450.
(16) Gunsior, M.; Ravel, J.; Challis, G. L.; Townsend, C. A. *Biochemistry* **2004**, *43*, 663−674.
(17) Shah, D. D.; Conrad, J. A.; Heinz, B.; Brownlee, J. M.; Moran, G. R. *Biochemistry* **2011**, *50*, 7694−7704.
(18) Fritze, I. M.; Linden, L.; Freigang, J.; Auerbach, G.; Huber, R.; Steinbacher, S. *Plant Physiol.* **2004**, *134*, 1388−13400.
(19) Neidig, M. L.; Kavana, M.; Moran, G. R.; Solomon, E. I. *J. Am. Chem. Soc.* **2004**, *126*, 4486−4487.
(20) Rundgren, M. *J. Biol. Chem.* **1977**, *252*, 5094−5099.
(21) Johnson-Winters, K.; Purpero, V. M.; Kavana, M.; Nelson, T.; Moran, G. R. *Biochemistry* **2003**, *42*, 2072−2080.
(22) He, P.; Conrad, J. A.; Moran, G. R. *Biochemistry* **2010**, *49*, 1998−2007.
(23) Raspail, C.; Graindorge, M.; Moreau, Y.; Crouzy, S.; Lefébvre, B.; Robin, A.; Dumas, R.; Matringe, M. *J. Biol. Chem.* **2011**, *286*, 26061−26070.
(24) Price, J. C.; Barr, E. W.; Tirupati, B.; Bollinger, J. M.; Krebs, C. *Biochemistry* **2003**, *42*, 7497−7508.
(25) Hoffart, L. M.; Barr, E. W.; Guyer, R. B.; Bollingern, J. M., Jr.; Krebs, C. *Proc. Natl. Acad. Sci. U.S.A.* **2006**, *103*, 14738−14743.
(26) Galonic, D. P.; Barr, E. W.; Walsh, C. T.; Bollinger, J. M., Jr.; Krebs, C. *Nat. Chem. Biol.* **2007**, *3*, 113−116.
(27) Shah, D. D.; Conrad, J. A.; Moran, G. R. *Biochemistry* **2013**, *52*, 6097−6107.

(28) Leinberger, R.; Hull, W.; Simon, H.; Rétey, J. *Eur. J. Biochem.* **1981**, *117*, 311−318.
(29) Eswar, N.; Marti-Renom, M.; Webb, B.; Madhusudhan, M.; Eramian, D.; Shen, M.; Pieper, U.; Sali, A. *Current Protocols in Bioinformatics*; John Wiley and Sons, Inc.: New York, 2006; Supplement 15, pp 5.6.1−5.6.30.
(30) Marti-Renom, M.; Stuart, A.; Fiser, A.; Sánchez, R.; Melo, F.; Sali, A. *Annu. Rev. Biophys. Biomol. Struct.* **2000**, *29*, 291−325.
(31) Sali, A.; Blundell, T. *J. Mol. Biol.* **1993**, *234*, 779−815.
(32) Fiser, A.; Do, R. K.; Sali, A. *Protein Sci.* **2000**, *9*, 1753−1773.
(33) Li, H.; Robertson, A.; Jensen, J. H. *Proteins* **2005**, *61*, 704−721.
(34) Bas, D. C.; Rogers, D. M.; Jensen, J. H. *Proteins* **2008**, *73*, 765−783.
(35) Duan, Y.; Wu, C.; Chowdhury, S.; Lee, M. C.; Xiong, G.; Zhang, W.; Yang, P.; R, Cieplak; Luo, R.; Lee, T.; Caldwell, J.; Wang, J.; Kollman, P. *J. Comput. Chem.* **2003**, *24*, 1999−2012.
(36) Jorgensen, W. L.; Chandrasekhar, J.; Madura, J. D.; Impey, R. W.; Klein, M. L. *J. Chem. Phys.* **1983**, *79*, 926−935.
(37) Case, D.; et al. *AMBER11*; University of California: San Francisco, 2010.
(38) Frisch, M.; et al. *Gaussian 09*, Revision A.1; Gaussian Inc.: Wallingford, CT, 2009.
(39) Becke, A. D. J. *Chem. Phys.* **1993**, *98*, 5648−5652.
(40) Lee, C.; Yang, W.; Parr, R. G. *Phys. Rev.* **1988**, *B37*, 785−789.
(41) Wang, J.; Cieplak, P.; Kollman, P. A. *J. Comput. Chem.* **2000**, *21*, 1049−1074.
(42) de Marothy, S. *XYZ-Viewer*, version 0.965, 2009; http://www.fysik.su.se/~marothy/.
(43) Grimme, S. *J. Comput. Chem.* **2006**, *27*, 1787−1799.
(44) Reiher, M.; Salomon, O.; Hess, B. A. *Theor. Chem. Acc.* **2001**, *107*, 48−55.
(45) Bhandarkar, M.; et al. *NAMD*, Version 2.7, User's Guide; University of Illinois: Urbana, IL, 2010.
(46) de Visser, S. P.; Shaik, S. *J. Am. Chem. Soc.* **2003**, *125*, 7413−7424.
(47) Borowski, T.; Bassan, A.; Siegbahn, P. E. M. *Inorg. Chem.* **2004**, *43*, 3277−3291.
(48) Bassan, A.; Blomberg, M. R. A.; Siegbahn, P. E. M. *Chem.—Eur. J.* **2003**, *9*, 4055−4067.
(49) Kumar, D.; Karamzadeh, B.; Sastry, G. N.; de Visser, S. P. *J. Am. Chem. Soc.* **2010**, *132*, 7656−7667.
(50) de Visser, S. P. *Chem.—Eur. J.* **2006**, *12*, 8168−8177.
(51) de Visser, S. P.; Ogliaro, F.; Shaik, S. *Chem. Commun.* **2001**, 2322−2323.
(52) Bassan, A.; Blomberg, M. R.; Siegbahn, P. E. M. *J. Biol. Inorg. Chem.* **2004**, *9*, 439−452.
(53) Rod, T. H.; Ryde, U. *J. Chem. Theory Comput.* **2005**, *1*, 1240−1251.